

1
2
3
4
5
6
7
8
9
10
11
12
13
14
15
16
17
18
19
20
21
22
23
24
25

UNIVERSITY OF CALIFORNIA
SANTA CRUZ

**AN INCLUSIVE SEARCH FOR THE DECAY OF A BOOSTED
HIGGS BOSON IN THE $H \rightarrow b\bar{b}$ CHANNEL WITH THE ATLAS
DETECTOR**

A dissertation submitted in partial satisfaction of the
requirements for the degree of
DOCTOR OF PHILOSOPHY

in

PARTICLE PHYSICS

by

Jacob Martin Pasner

October 2019

The Dissertation of Jacob Martin Pasner
is approved:

Professor Jason Nielsen, Chair

Professor Abraham Seiden

Professor Michael Hance

Dean Lori Kletzer
Vice Provost and Dean of Graduate Studies

Copyright © by

Jacob Martin Pasner

2019

31 **Table of Contents**

| | | |
|----|---|------------|
| 32 | List of Figures | vii |
| 33 | List of Tables | ix |
| 34 | Abstract | x |
| 35 | Dedication | xi |
| 36 | Acknowledgments | xii |
| 37 | 1 Introduction | 1 |
| 38 | I Theoretical Motivations and the Standard Model | 2 |
| 39 | 2 The Standard Model and Beyond | 3 |
| 40 | 2.1 The Standard Model | 4 |
| 41 | 2.1.1 Bosons | 5 |
| 42 | 2.1.2 Fermions | 8 |
| 43 | 2.2 Quantum Electrodynamics | 8 |
| 44 | 2.3 Quantum Chromodynamics | 11 |
| 45 | 2.4 Spontaneous Symmetry Breaking | 11 |

| | | | |
|----|-----------|---|-----------|
| 46 | 2.5 | The Higgs Mechanism | 11 |
| 47 | 2.6 | Parton Distribution Function | 11 |
| 48 | II | Experimental Apparatus and Associated Facilities | 12 |
| 49 | 3 | The Large Hadron Collider | 13 |
| 50 | 3.1 | Particle Incjecton Chain | 14 |
| 51 | 3.2 | LHC layout and design | 16 |
| 52 | 3.3 | Performance | 19 |
| 53 | 3.4 | Pile-up at the LHC | 21 |
| 54 | 4 | The ATLAS Detector | 23 |
| 55 | 4.1 | ATLAS Coordinate System | 26 |
| 56 | 4.2 | Tracking with the Inner Detector | 30 |
| 57 | 4.2.1 | Pixel Detector | 32 |
| 58 | 4.2.2 | Semiconductor Tracker | 32 |
| 59 | 4.2.3 | Transition Radiation Tracker | 33 |
| 60 | 4.3 | Calorimetry | 34 |
| 61 | 4.3.1 | Electromagnetic Calorimeter | 35 |
| 62 | 4.3.2 | Hadronic Calorimeter | 37 |
| 63 | 4.4 | Muon Spectrometer | 39 |
| 64 | 5 | Boosted Higgs at the LHC | 42 |
| 65 | 5.1 | Physics beyond the Stnadard Model | 43 |
| 66 | 5.2 | Higgs Production Mechanisms | 43 |
| 67 | 5.3 | Branching Ratios | 43 |
| 68 | 5.4 | Discovery | 43 |

| | | | |
|----|------------|---|-----------|
| 69 | 5.5 | Fermion Decay Modes | 43 |
| 70 | 5.6 | Boosted Higgs | 43 |
| 71 | III | The HbbISR Analysis | 44 |
| 72 | 6 | Data and Simulation Preparation | 45 |
| 73 | 6.1 | Data Used | 45 |
| 74 | 6.2 | Monte Carlo Samples | 45 |
| 75 | 7 | Physics Object Selection | 46 |
| 76 | 7.1 | Calorimeter Jets | 47 |
| 77 | 7.2 | Track Jets | 47 |
| 78 | 7.3 | Fat Jets | 47 |
| 79 | 7.4 | B-tagged Jets | 47 |
| 80 | 7.5 | Muons | 47 |
| 81 | 7.6 | Overlap Removal | 47 |
| 82 | 8 | Event Selection | 48 |
| 83 | 8.1 | Selected Triggers | 48 |
| 84 | 8.2 | Pre-selection Studies | 48 |
| 85 | 8.3 | Signal Selection | 48 |
| 86 | 8.4 | Optimisation | 48 |
| 87 | 9 | Background Estimation | 49 |
| 88 | 9.1 | Multi-jet QCD estimation | 49 |
| 89 | 9.2 | $t\bar{t}$ control region | 49 |
| 90 | 9.3 | Single top estimation | 49 |
| 91 | 9.4 | Hadronic vector boson channel | 49 |

| | | |
|-----|---|-----------|
| 92 | 10 Systematic Uncertainties | 50 |
| 93 | 10.1 Theoretical Uncertainties | 50 |
| 94 | 10.2 Experimental Uncertainties | 50 |
| 95 | 11 Statistical Fit | 51 |
| 96 | 11.1 Profile Likelihood Function | 51 |
| 97 | 11.2 Fit Configuration | 51 |
| 98 | 11.3 Statistical Tests | 51 |
| 99 | 12 Results | 52 |
| 100 | 12.1 Expectations | 52 |
| 101 | 12.2 Statistical Analysis Results | 52 |
| 102 | 12.3 Measurements and Limits | 52 |
| 103 | IV Conclusion | 53 |
| 104 | 13 Conclusion | 54 |
| 105 | Bibliography | 54 |
| 106 | A Hadronic Vqq Sherpa Studies | 57 |

107 List of Figures

| | | | |
|-----|-----|--|----|
| 108 | 2.1 | Summary of several Standard Model total and fiducial production cross | |
| 109 | | section measurements, corrected for leptonic branching fractions, com- | |
| 110 | | pared to the corresponding theoretical expectations. All theoretical ex- | |
| 111 | | pectations were calculated at NLO or higher. The dark-color error bar | |
| 112 | | represents the statistical uncertainty. The lighter-color error bar repre- | |
| 113 | | sents the full uncertainty, including systematics and luminosity uncer- | |
| 114 | | tainties. The data/theory ratio, luminosity used and reference for each | |
| 115 | | measurement are also shown. Uncertainties for the theoretical predictions | |
| 116 | | are quoted from the original ATLAS papers. They were not always eval- | |
| 117 | | uated using the same prescriptions for PDFs and scales. The Wgamma | |
| 118 | | and Zgamma theoretical cross-sections have non-perturbative corrections | |
| 119 | | applied to the NNLO fixed order calculations (PRD 87, 112003 (2013)). | |
| 120 | | Not all measurements are statistically significant yet. | 6 |
| 121 | 2.2 | Table of all observed fundamental particles of the current Standard Model. | 7 |
| 122 | 3.1 | CERN accelerator complex | 15 |
| 123 | 3.2 | Labeled diagram of all the experiments at the LHC indicating the counter | |
| 124 | | circulating beams and points of interest along the circumference of the | |
| 125 | | accelerator. | 17 |
| 126 | 3.3 | Depiction of a LHC dipole magnet 2-in-1 design labeling the major com- | |
| 127 | | ponents | 18 |
| 128 | 3.4 | Luminosity is monitored as both a running total known as the Integrated | |
| 129 | | Luminosity as depicted in (a) and as an instantaneous quantity as shown | |
| 130 | | in (b) | 21 |
| 131 | 3.5 | Pileup for data taking periods 2015 - 2018 | 22 |

| | | | |
|-----|------|--|----|
| 132 | 4.1 | [3] Here we see a cut-away side view of the ATLAS detector with the | |
| 133 | | major components labeled. Note that within each of these labeled com- | |
| 134 | | ponents there may exist multiple different detector technologies. For scale | |
| 135 | | two people in red are shown standing between the disk muon chambers | |
| 136 | | on the left side of the figure. | 24 |
| 137 | 4.2 | This slice of the ATLAS detector depicts how different particles interact | |
| 138 | | with each component of the detector it crosses. A dashed line indicates | |
| 139 | | no interaction while a solid line indicates interaction. Electrons (yel- | |
| 140 | | low/green) and charged hadrons (red) interact with the tracker and curve | |
| 141 | | in the solenoid's magnetic field. Electrons and photons (yellow/green) are | |
| 142 | | absorbed by the Electromagnetic calorimeter. All hadrons (red/yellow) | |
| 143 | | are absorbed by the Hadronic calorimeter. The muons (orange) curve in | |
| 144 | | both the solenoid and torroid magnetic fields before exiting the detector. | |
| 145 | | Finally, the neutrinos (white) pass through the entire detector without | |
| 146 | | interacting. | 27 |
| 147 | 4.3 | [4] A cartoon view of the the LHC from above showing the SPS, LHC | |
| 148 | | and the four main experiments of the LHC: ATLAS, CMS, LHCb, and | |
| 149 | | ALICE. The standard cartesian coordinate system is shown with its origin | |
| 150 | | at the ATLAS interaction point, the positive x -axis towards the center | |
| 151 | | of the LHC, the positive y -axis pointing upwards, and the positive z -axis | |
| 152 | | pointing along the beamline towards the "A-side" | 28 |
| 153 | 4.4 | Modified from [4] this cartoon represents a selection of pseudorapidity | |
| 154 | | (η) values overlaid with some cartesian coordinates (dashed black lines). | |
| 155 | | The redlines are drawn for $\eta = \pm 0.5, 1.0, 3.0$ | 29 |
| 156 | 4.5 | [5] Diagram of inner detector | 30 |
| 157 | 4.6 | [8] Schematic of the Inner Detector including eta lines. Each component | |
| 158 | | shown is cylindrically symmetric leading to a multi-layered detector. . . | 31 |
| 159 | 4.7 | [3] A cutaway diagram of ATLAS's sampling calorimeters | 34 |
| 160 | 4.8 | [3] Sketch of LAr EMC barrel module where the lead and liquid argon | |
| 161 | | layers are visible in an accordion like geometry. Looking from the fore- | |
| 162 | | ground to the back there are 3 different types of cells visible. | 36 |
| 163 | 4.9 | [3] Schematic of a tile calorimeter module including a depiction of the con- | |
| 164 | | nection between the scintillator tile to the photomultiplier via a wavelength- | |
| 165 | | shifting fibre. | 38 |
| 166 | 4.10 | [3] A cut-away diagram of the ATLAS muon system and its many sub- | |
| 167 | | detectors. | 40 |

168 List of Tables

Abstract

170 An Inclusive Search for the decay of a Boosted Higgs boson in the $H \rightarrow b\bar{b}$
171 channel with the ATLAS detector

172 by

173 Jacob Martin Pasner

174 Abstract placeholder

| | |
|-----|------------|
| 175 | Dedication |
| 176 | Dedication |
| 177 | Dedication |

Acknowledgments

179 Chapter 1

180 Introduction

181 Every dissertation should have an introduction. You might not realize it, but the
182 introduction should introduce the concepts, backgrouand, and goals of the dissertation.

183

Part I

184

Theoretical Motivations and the

185

Standard Model

Chapter 2

The Standard Model and Beyond

The Standard Model (SM) of Particle Physics is humanities best "guess" at the force laws that describe the observed behavior of all particles in our universe. Its formulation is a collection of Quantum Field Theories (QFT) that describe the following interactions of elementary matter in Nature: the electromagnetic force, the weak nuclear force and the strong nuclear force. Gravity is noticeably absent as currently there is no viable quantum theory for observed gravitational effects. The Glashow-Weinberg-Salam theory of Quantum Electrodynamics (QED) describes the electromagnetic and weak forces, while Quantum Chromodynamics (QCD) describes the strong force. These theories form the following symmetry group of the Standard Model.

$$\underbrace{\mathrm{SU}_C(3)}_{\mathrm{QCD}} \otimes \underbrace{\mathrm{SU}_L(2) \otimes \mathrm{U}_Y(1)}_{\mathrm{QED}}. \quad (2.1)$$

197 The gauge principle states that the SM Lagrangian and its predictions must be invariant
198 under local transformations using an operator from any of these constituent groups.
199 Thus, any theory must only include transformations and terms that maintain the local
200 invariance of the complete Lagrangian. In particular, this requirement was violated
201 by any attempt to include an explicit mass term for the Gauge Bosons of QED and
202 for all fermions. Around 1960 a possible solution to this lack of mass was proposed
203 in the form of the spontaneous breaking of the ElectroWeak symmetry, now known as
204 the Higgs mechanism. In the following sections I will go into more detail about the
205 Lagrangian formalism of the Standard Model, QCD, QED and this recently verified
206 Higgs Mechanism.

207 **2.1 The Standard Model**

208 At the turn of the 20th century our understanding of the constituent matter of the uni-
209 verse was limited to what we could see with microscopes and imply from the observations
210 of light and electricity, giving us evidence for both the photon and the electron. In the
211 first half of the century we discovered the field of subatomic physics with Rutherford's
212 1911 gold foil scattering experiment, and Dirac successfully demonstrated the quantiza-
213 tion of the electromagnetic field, the first step towards a fully Gauge Invariant Quantum
214 Field Theory. In the second half we literally delved deeper, discovering that the nucleus
215 contained structure and extended our theories to include the the complex mechanics of
216 quarks and gluons. With the discovery of the Higgs in 2013 the Standard Model has

217 become an irrefutable framework as can be seen in the high level of agreement between
218 theory and experiment in figure 2.1.

219 The QCD and QED theories predict two classes of particles: fermions and bosons shown
220 in figure 2.2. These particles represent the quanta of the quantum fields of the Standard
221 Model and the mediators of the fundamental forces of Nature.

222 2.1.1 Bosons

223 These spin-1 particles are known as the vector gauge bosons and are the force carriers
224 of the SM. The most commonly known is the electromagnetic force's un-charged and
225 massless photon (γ) which interacts with all charged particles and is often referred to
226 as "light". The weak nuclear force is involved in nuclear interactions such as beta
227 decays and is carried by 3 bosons all of which have mass and couple to all fermions;
228 the W^\pm bosons, which mediate the charged weak nuclear interaction and allow for
229 flavor changing currents; and the Z boson which mediates the neutral weak nuclear
230 interaction. Finally we have 8 massless gluons which mediate the strong nuclear force
231 and only interact with fermions with a "color" charge such as the quarks contained
232 inside the nucleus. The only spin-0 boson, the Higgs Boson (h) is the key to generating
233 mass terms in the SM Lagrangian for the massive Gauge Bosons and for fermions. This
234 is done through the so called Higgs Mechanism and is discussed in more detail in section
235 2.5.

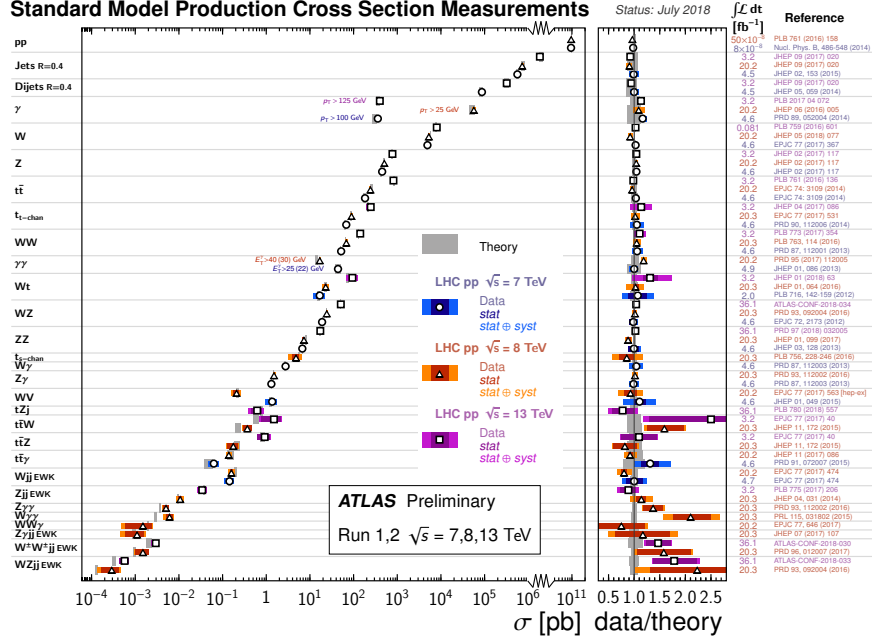


Figure 2.1: Summary of several Standard Model total and fiducial production cross section measurements, corrected for leptonic branching fractions, compared to the corresponding theoretical expectations. All theoretical expectations were calculated at NLO or higher. The dark-color error bar represents the statistical uncertainty. The lighter-color error bar represents the full uncertainty, including systematics and luminosity uncertainties. The data/theory ratio, luminosity used and reference for each measurement are also shown. Uncertainties for the theoretical predictions are quoted from the original ATLAS papers. They were not always evaluated using the same prescriptions for PDFs and scales. The $W\gamma$ and $Z\gamma$ theoretical cross-sections have non-perturbative corrections applied to the NNLO fixed order calculations (PRD 87, 112003 (2013)). Not all measurements are statistically significant yet.

Standard Model of Elementary Particles

| three generations of matter (fermions) | | | | | | interactions / force carriers (bosons) | |
|--|---------------------------------|----------------------------------|----------------------------------|---------------------------------|----------------------------------|--|--|
| I | | II | | III | | | |
| mass | $\approx 2.2 \text{ MeV}/c^2$ | $\approx 1.28 \text{ GeV}/c^2$ | $\approx 173.1 \text{ GeV}/c^2$ | 0 | $\approx 124.97 \text{ GeV}/c^2$ | | |
| charge | $\frac{2}{3}$ | $\frac{2}{3}$ | $\frac{2}{3}$ | 0 | 0 | | |
| spin | $\frac{1}{2}$ | $\frac{1}{2}$ | $\frac{1}{2}$ | 1 | 0 | | |
| QUARKS | | | | | | | |
| | up | charm | top | gluon | higgs | | |
| | $\approx 4.7 \text{ MeV}/c^2$ | $\approx 96 \text{ MeV}/c^2$ | $\approx 4.18 \text{ GeV}/c^2$ | 0 | | | |
| | $-\frac{1}{3}$ | $-\frac{1}{3}$ | $-\frac{1}{3}$ | 0 | | | |
| | $\frac{1}{2}$ | $\frac{1}{2}$ | $\frac{1}{2}$ | 1 | | | |
| | | | | | | | |
| | down | strange | bottom | photon | | | |
| LEPTONS | $\approx 0.511 \text{ MeV}/c^2$ | $\approx 105.66 \text{ MeV}/c^2$ | $\approx 1.7768 \text{ GeV}/c^2$ | $\approx 91.19 \text{ GeV}/c^2$ | | | |
| | -1 | -1 | -1 | 0 | | | |
| | $\frac{1}{2}$ | $\frac{1}{2}$ | $\frac{1}{2}$ | 1 | | | |
| | | | | | | | |
| | electron | muon | tau | Z boson | | | |
| | $< 2.2 \text{ eV}/c^2$ | $< 0.17 \text{ MeV}/c^2$ | $< 18.2 \text{ MeV}/c^2$ | $\approx 80.39 \text{ GeV}/c^2$ | | | |
| | 0 | 0 | 0 | ± 1 | | | |
| | $\frac{1}{2}$ | $\frac{1}{2}$ | $\frac{1}{2}$ | 1 | | | |
| | | | | | | | |
| | electron neutrino | muon neutrino | tau neutrino | W boson | | | |

Figure 2.2: Table of all observed fundamental particles of the current Standard Model.

2.1.2 Fermions

These spin-1/2 particles can be further broken up into two distinct families of particles, the leptons and the quarks, both of which contain three "generations" each with an "up" and "down" type particle. The leptons "up" type members are the electrically charged electron (e), muon (μ) and tau (τ) while the "down" type are their electrically neutral counterparts ν_e , ν_μ , ν_τ . The quarks "up" type members are the up (u), charm (c), and top (t) each with a $+2/3$ elementary charge, while the "down" type members are the down (d), strange (s), and bottom (b) all of which have a $-1/3$ elementary charge. Each quark carries a "color" charge thus allowing them to participate in strong force interactions. Due to the observed color confinement of the strong force these quarks are only observed in colorless bound states known as "mesons" (1 quark and 1 anti-quark) and "baryons" (an odd number of quarks and anti-quarks). All of the above fermions have an anti-particle partner which has the opposite electrical charge but is otherwise identical.

2.2 Quantum Electrodynamics

In the SM the Electromagnetic and Weak nuclear forces are unified into the Electroweak interaction which is represented by the $SU(2)_L \times U(1)_Y$ gauge group. The L represents the physical observable that the Weak interaction, and thus the $SU(2)$ transformation, only acts on left handed particle states. The Y states that this is the $U(1)$ symmetry

255 for the weak hypercharge Y instead of the electromagnetic charge. The particle states
 256 for these interactions are solutions to the Dirac equation and are represented as Dirac
 257 spinor doublets (Ψ_L) for the left handed states, and as Dirac spinor singlets (Φ_R) for
 258 the right handed states. Thus when a general transformation from the Electroweak
 259 gauge group is applied to the left handed spinor doublet you get equation 2.2

$$\Psi_L \rightarrow \Psi'_L = \exp \left(\underbrace{ig' \frac{Y_L}{2} \zeta(x)}_{U(1)_Y} + \underbrace{ig_W \boldsymbol{\alpha}(x) \cdot \mathbf{T}}_{SU(2)_L} \right) \Psi_L. \quad (2.2)$$

260 For the right handed spinor singlet the $SU(2)_L$ doesn't contribute and you get equation
 261 2.3

$$\Phi_R \rightarrow \Phi'_R = \exp \left(\underbrace{ig' \frac{Y_R}{2} \zeta(x)}_{U(1)_Y} \right) \Phi_R. \quad (2.3)$$

262 We can see that these local gauge transformations have introduced space-time depended
 263 terms $\boldsymbol{\alpha}$ and ζ into our electroweak Lagrangian. Due to the derivatives contained within
 264 the kinetic term of this lagrangian, this new configuration would introduce additional
 265 terms, thus violating our required local gauge invariance. Luckily, we can remove these
 266 additional terms by replacing the standard derivative (∂_μ) with th covariant derivative
 267 (D_μ) as seen in equation 2.4 for the left handed states and 2.5 for the right handed

268 states.

$$D_\mu = \partial_\mu - \underbrace{\frac{1}{2}ig'B_\mu Y_L}_{U(1)_Y} - \underbrace{\frac{1}{2}ig_W \mathbf{W}_\mu \cdot \boldsymbol{\tau}}_{SU(2)_L} \quad (2.4)$$

$$D_\mu = \partial_\mu - \underbrace{\frac{1}{2}ig'B_\mu Y_R}_{U(1)_Y} \quad (2.5)$$

269 Here we see two new gauge fields; B_μ the weak hypercharge field and \mathbf{W}_μ the charged
 270 weak field. The form of these fields is chosen such that the final Lagrangian is invariant
 271 under $SU(2)_L \times U(1)_Y$ transformations, and thus we have restored gauge invariance for
 272 the kinetic term of our electroweak Lagrangian! Inserting these new definitions into the
 273 Lagrangian for the spinor field Ψ which satisfies the free-particle Dirac equation we get

$$\mathcal{L} = i\bar{\Psi}\gamma^\mu \left(\partial_\mu - \frac{1}{2}ig'B_\mu Y_L - \frac{1}{2}ig_W \mathbf{W}_\mu \cdot \boldsymbol{\tau} \right) \Psi + i\Phi_R\gamma^\mu \left(\partial_\mu - \frac{1}{2}ig'B_\mu Y_R \right) \Phi_R \quad (2.6)$$

274 Wavefunction Transformation Covariant Derivative Lagrangian Identify Terms

275 In the SM the electromagnetic and weak nuclear forces are unified into the electroweak
 276 interaction which . . .

277 Quantum Electrodynamics is the first model created in the QFT image.

278 **2.3 Quantum Chromodynamics**

279 Quantum chromodynamics is super wack

280 **2.4 Spontaneous Symmetry Breaking**

281 Spontaneous symmetry breaking occurs when a system loses an inherent symmetry in
282 order to attain a lower energy configuration.

283 **2.5 The Higgs Mechanism**

284 The Higgs Mechanism is the system by which particles attain mass through the spon-
285 taneous breaking of the Higgs potential, thus causing all particles it interacts with to
286 have mass.

287 **2.6 Parton Distribution Function**

288 Before QFT the proton was thought to be a hard ball containing no smaller constituents.
289 However, we know now that that the strong field inside the proton allows for any strong
290 object to exist with some probability which changes based off of the total energy of the
291 proton. This behavior is represented then by a Probability Distribution Function.

292

Part II

293

Experimental Apparatus and

294

Associated Facilities

Chapter 3

The Large Hadron Collider

Located 100 meters under the Swiss / French boarder lies the 26.7 kilometer Large Hadron Collider (LHC) [1]. The culmination of a huge international collaboration, this apparatus is used to produce proton and heavy ion collisions for observation by the four major experiments at the LHC: ATLAS, CMS, LHCb, and ALICE. The system was designed for a maximum center-of-mass energy of $\sqrt{s} = 14$ TeV and a peak instantaneous luminosity of $L = 10^{34} \text{cm}^{-2} \text{s}^{-1}$.

The first LHC workshop was held in 1984 in Lausanne at the European Organization for Nuclear Reserach (CERN) [2]. The nearly 30 year old case for a machine that would push towards the discovery of the elusive Higgs Boson was presented using the existing CERN accerlerator facilities and the Large Electron Positron (LEP) collider tunnel. The proposal became reality on September 10, 2008 when the first proton beams were circulated, only to have calamity strike 9 days later in the form of a catastrophic

309 electrical fault. The repairs and improvements lasted until November 2009 when the
310 LHC restarted. Since then this modern marvel has worked wonderfully and, as hoped,
311 lead to the discovery of the Higgs Boson by the CMS and ATLAS collaborations July
312 4, 2013.

313 The following chapter provides a brief introduction to the worlds most powerful accel-
314 erator starting with the little red bottle of hydrogen in building XXX, and ending with
315 the interaction point where protons collide at the highest energies ever produced.

316 **3.1 Particle Injecton Chain**

317 We begin with the most common element in the Universe, hydrogen, as our source of
318 protons. A bottle of hydrogen gas provides 100 microsecond pulses of raw H_2 which
319 is then injected into a Duoplasmatron. There, a strong electric field and free elctrons
320 from a cathode ionize the molecule into bare H^+ aka a proton! These protons are
321 then accelerated by a 90kV field, leaving the Duoplasmatron with 1.4% speed of light
322 ($\sim 4000\text{km/s}$) or, in relativistic units, about 83KeV. The bare protons are then fed
323 into the accelerating RadioFrequency (RF) cavities of Linear Accelerator 2 (LINAC2).
324 Inside, conductors charged by a powerful oscillating electromagnetic field accelerate the
325 protons resulting in a 50MeV energy. Along the way, small quadrupole magnets shape
326 the proton packet insuring they remain in a tight beam. This pattern of accleration
327 with RF cavities and shaping/turnig with magnets is then repeated with CERN's first

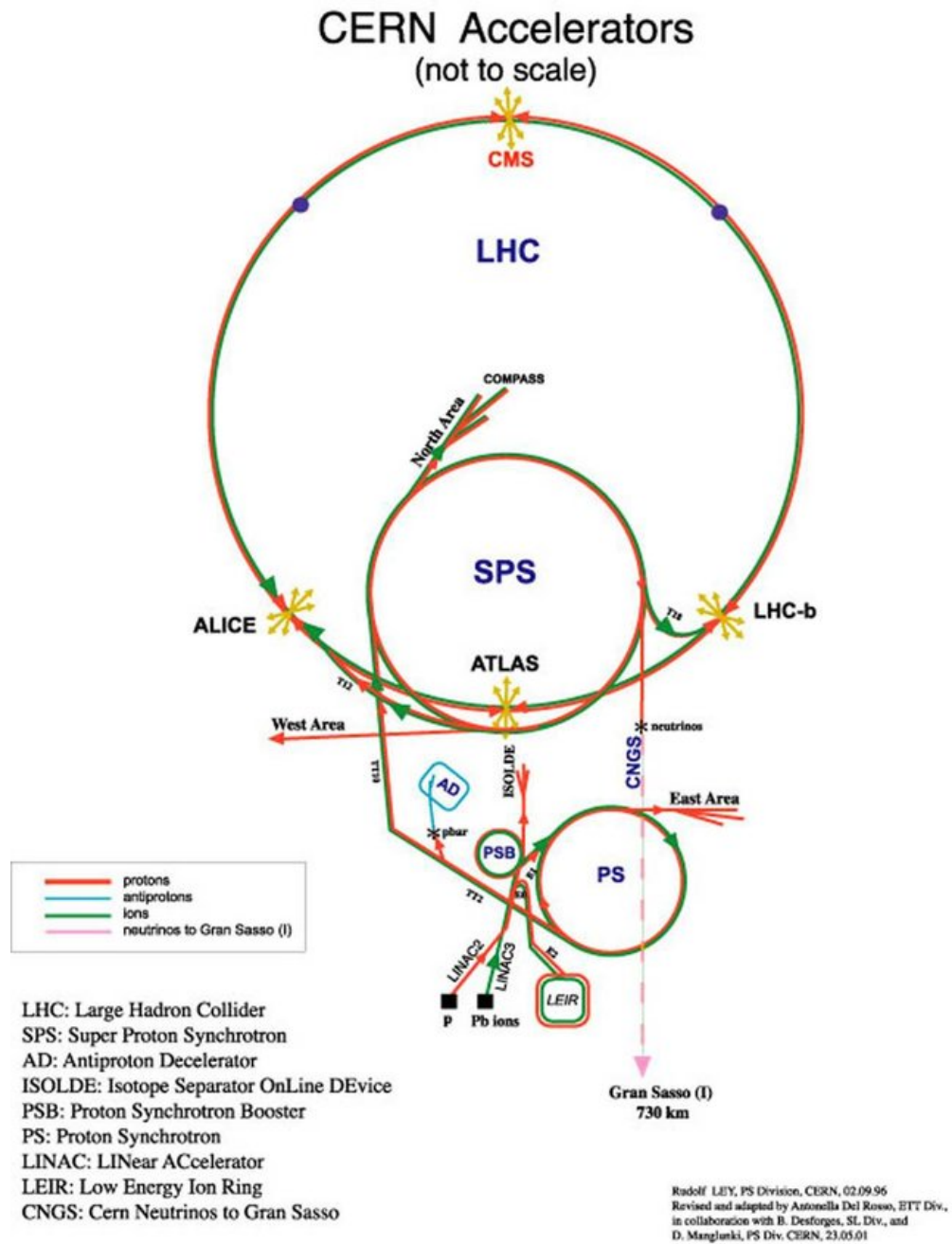


Figure 3.1: CERN accelerator complex

328 synchrotron, the Proton Synchrotron (PS) rendering a 1.4 GeV beam. The final step
329 before the LHC comes with the Super Proton Synchrotron where the same technologies
330 are implemented to produce 450 GeV protons, ready for injection into the LHC. A
331 diagrammatic representation of this chain can be seen in figure 3.1

332 In order to produce proton-proton collisions the LHC uses two beams circulating in
333 opposite directions. The beams are not continuous, but instead consist of bunches, or
334 buckets, of $\mathcal{O}(10^{11})$ protons with a spacing of 25ns. Given the LHC circumference this
335 allows for 3564 buckets, however only 2808 are filled per beam due to safety requirements
336 and injection limitations. Each beam takes 4 minutes and 20 seconds to fill and then an
337 additional 20 minutes to for the protons to reach their maximum energy of 7 TeV TeV,
338 or 99.99999991% the speed of light! Under normal operating conditions these beams
339 can be used for many hours.

340 **3.2 LHC layout and design**

341 While often depicted as a perfect circle the LHC is in reality an octagon with rounded
342 edges, called arcs, as can be seen in figure 3.2. Here you can see the counter circulating
343 beams of protons depicted in red and blue. These beams are focused and collided at
344 the 4 dedicated interaction points at rates of up to 40 MHz. Two of these points are
345 occupied by the ATLAS and CMS experiments, both of which are high luminosity,
346 multi-purposed experiments.

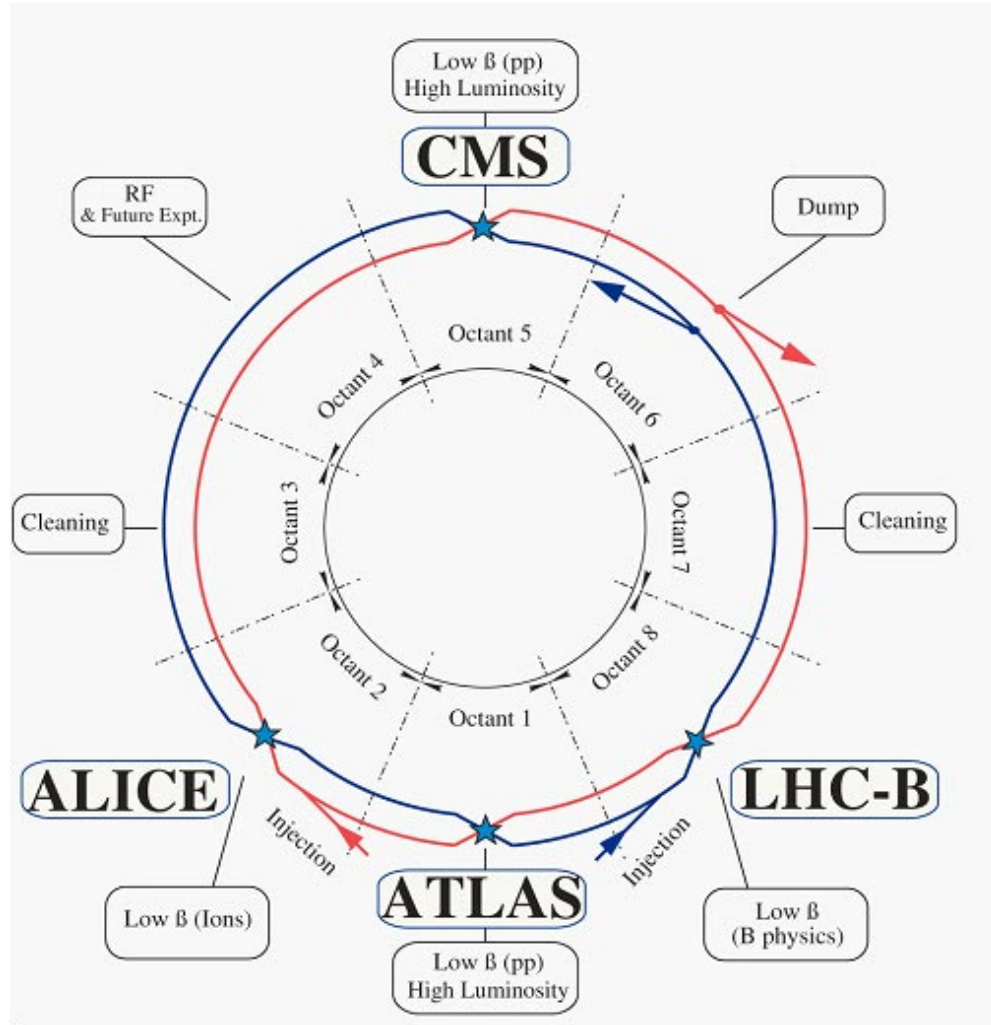


Figure 3.2: Labeled diagram of all the experiments at the LHC indicating the counter circulating beams and points of interest along the circumference of the accelerator.

347 The exact design of the tunnel is due to the experimental constraints of the original
 348 machine for which it was built, the Large Electron Positron (LEP) Collider. For the
 349 $\sim 2,000$ times lighter electron the maximum energy was limited by the synchrotron
 350 radiation, proportional to $\frac{1}{m^4}$, requiring long straight sections of accelerating RF cavities
 351 to recouperate the lost energy. Given that this effect is $\mathcal{O}(10^{13})$ times smaller for the
 352 proton the LHC is instead limited by our ability to design and construct magnets strong
 353 enough to bend the beam given the already determined curvature of the 8 arcs.

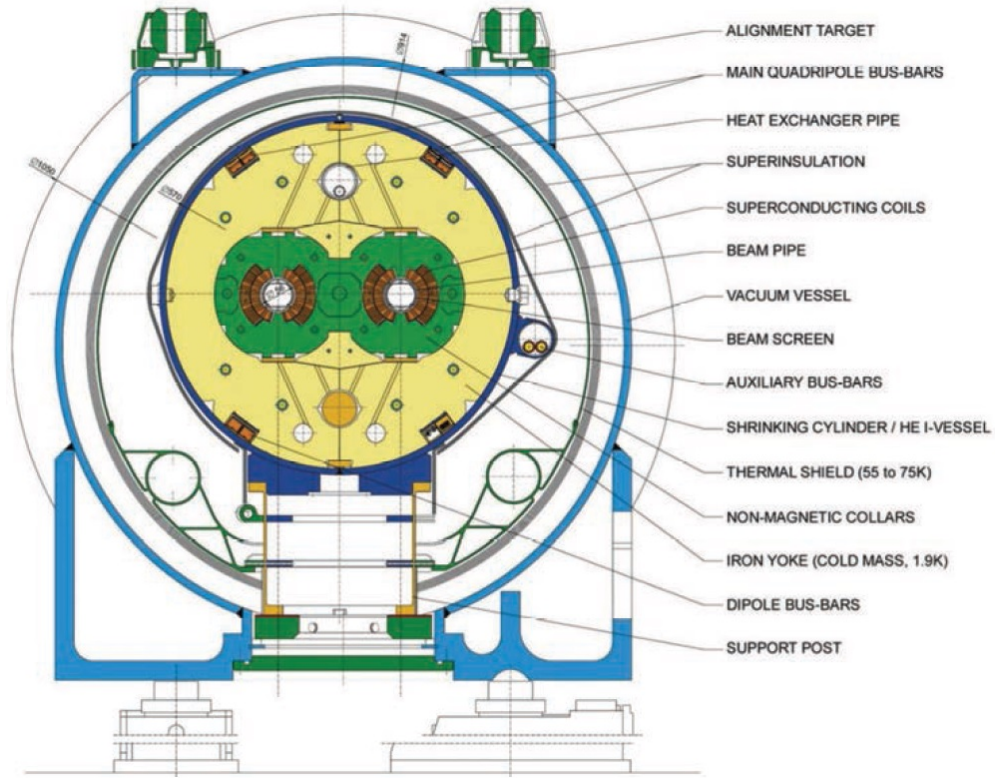


Figure 3.3: Depiction of a LHC dipole magnet 2-in-1 design labeling the major components

354 The oppositely circulating beams must each have their own ring and magnetic field
355 which lead to the creation of a twin-bore (i.e. "two-in-one") magnet design, a cross
356 section of which can be seen in figure 3.3. These magnets are constructed using NbTi
357 superconductors which are cooled to 2K using superfluid helium. These magnets are
358 designed to provide the needed 8.33 T magnetic field required to bend the beams at the
359 design beam energy of 7 TeV. In total 1231 of these 15 m long bending dipole magnets
360 are used, in association with 392 5-7m long quadrupole magnets which are responsible
361 for keeping the proton bunches in a tight beam by squeezing them either horizontally
362 or vertically.

363 **3.3 Performance**

364 Since the begining of its stable running in 2010 the LHC has performed well, even
365 exceeding our expectations. While the experiment itself is incredibly complex, the
366 performance of the machine, for the purposes of our analysis, can be reduced to two
367 numbers; the familiar center of mass energy of the beams and a less common quantity
368 known as the integrated luminosity.

369 For particle physics the integrated luminosity is proportional to the total number of
370 collisions recorded during a specified time period, while the instantaneous luminosity is
371 proportional to the bunch crossing rate along with the cross section of a proton-proton
372 interaction and represents the potential number of collisions per second. Knowing this

we can see that the integrated luminosity, L_{int} is simply the integral of the instantaneous luminosity $L_{inst.}$ for a choosen data period as seen in equation 3.1.

$$L_{int} = \int L_{inst.} dt \quad (3.1)$$

For a standard Gaussian beam, $L_{inst.}$ can be written as

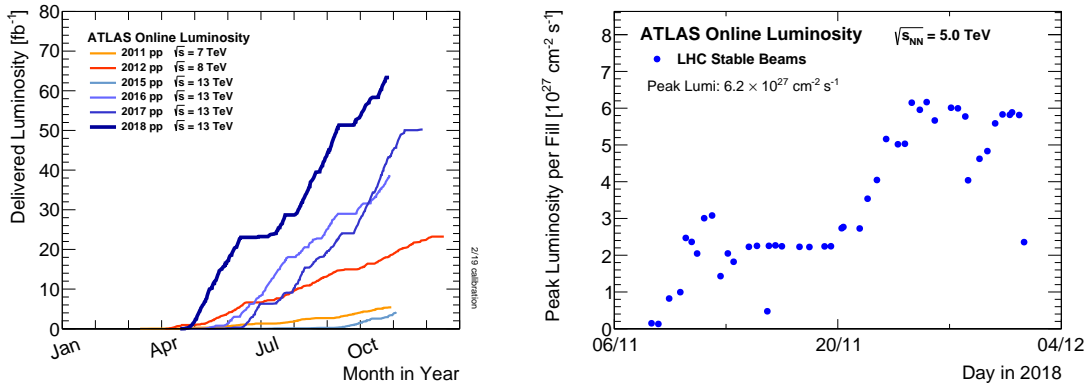
$$L = \frac{N_b^2 n_b f_{rev} \gamma_r}{4\pi \epsilon_n \beta^*} F \quad (3.2)$$

where N_b is the number of particles per bunch, n_b the number of bunches per beam, f_{rev} the revolution frequency, γ_r the relativistic gamma factor, ϵ_n the normalized transverse beam emittance, β^* the beta function at the collision point, and F the geometric luminosity reduction factor due to the crossing angle at the interaction point given by

$$F = \left(1 + \left(\frac{\theta_c \sigma_z}{2\sigma^*} \right)^2 \right)^{-1/2} \quad (3.3)$$

where θ_c is the full crossing angle at the interaction point, σ_z is the RMS bunch length, and σ^* is the transverse RMS beam size at the interaction point.

For the ATLAS experiment the integrated luminosity for each year can be seen in figure 3.4a as well as an example of the instantaneous luminosity for the choosen year in figure 3.4b.



(a) Integrated Luminosity 2011 - 2018 (b) 2018 Peak Instantaneous Luminosity

Figure 3.4: Luminosity is monitored as both a running total known as the Integrated Luminosity as depicted in (a) and as an instantaneous quantity as shown in (b)

3.4 Pile-up at the LHC

Given the large number of protons per bunch and the cross-section of a proton-proton interaction, the probability to observe multiple interactions per bunch crossing is quite high. These multiple-interaction are known as pile-up, μ or the time averaged representation $\langle\mu\rangle$, and come in two different forms:

1. **In-time pile-up:** These are the other proton-proton collisions that occur during the same bunch crossing as the primary interaction that caused the Data Acquisition (DAQ) system to trigger. These are the standard extra interactions we expect to observe as stated above.
2. **Out-of-time pile-up:** These are interactions that occur either before or after a

395 bunch crossing that causes the DAQ to trigger. This effect is generally due to the
 396 long integration times of some detector electronics.

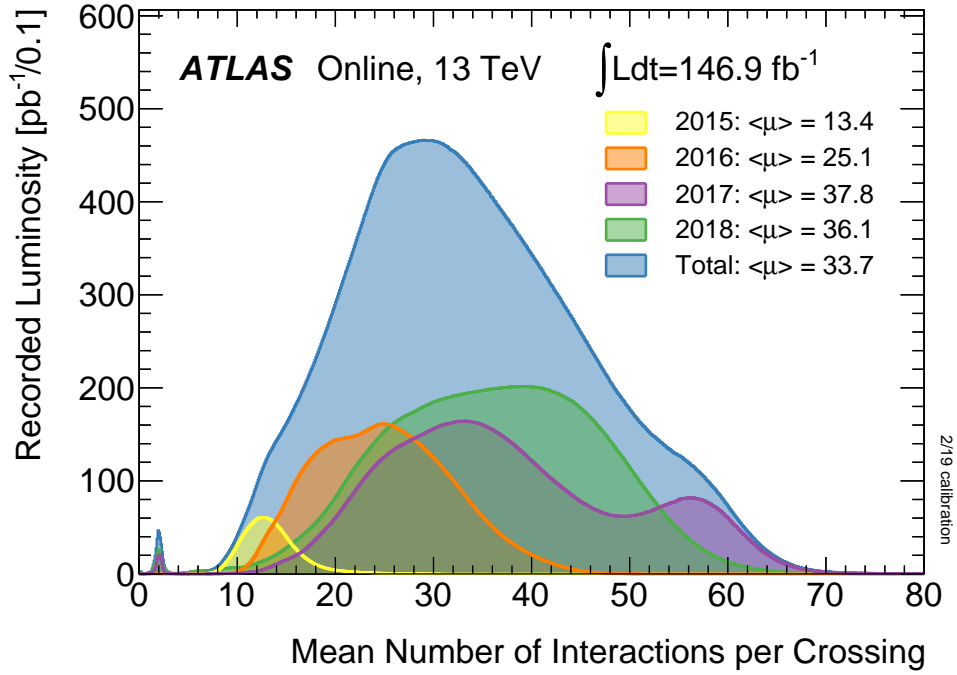


Figure 3.5: Pileup for data taking periods 2015 - 2018

397 The pile-up profile for past years can be seen in figure 3.5. The width of this distributino
 398 is due a combination of Poissonian statistics, the decrease in number of protons per bunch
 399 over the lifetime of a single run, and optimization tweaks to the beam's profile during
 400 runtime. Understanding and eliminating the noise from these pile-up events is crucial
 401 to reconstructing physics variables to represent the primary interaction we hope to
 402 observe.

403 Chapter 4

404 The ATLAS Detector

405 Given the immense energies available at the LHC, and the veritable zoo of particles we
406 are trying to detect, we require a general-purpose experiment in order to fully exploit
407 the full range of physics opportunities provided. Two international collaborations rose
408 to this challenge, the CMS (Compact Muon Solenoid) and ATLAS (A Torroidal LHC
409 ApparatuS) experiments. While both have similar physics goals and each of them
410 strengths and weaknesses, this dissertation will focus on the ATLAS experiment and
411 the intricacies of its three main sub-detectors and two massive magnet systems depicted
412 in figure 4.1.

413 Originally proposed in 1994 the ATLAS experiment was completed in 2008. On July
414 4th, 2012 in a joint announcement the ATLAS and CMS experiments announced the
415 discovery of the long predicted Higgs Boson. The collaboration now boasts over 3000
416 physicists from 175 institutions spread across 38 countries and continues to probe

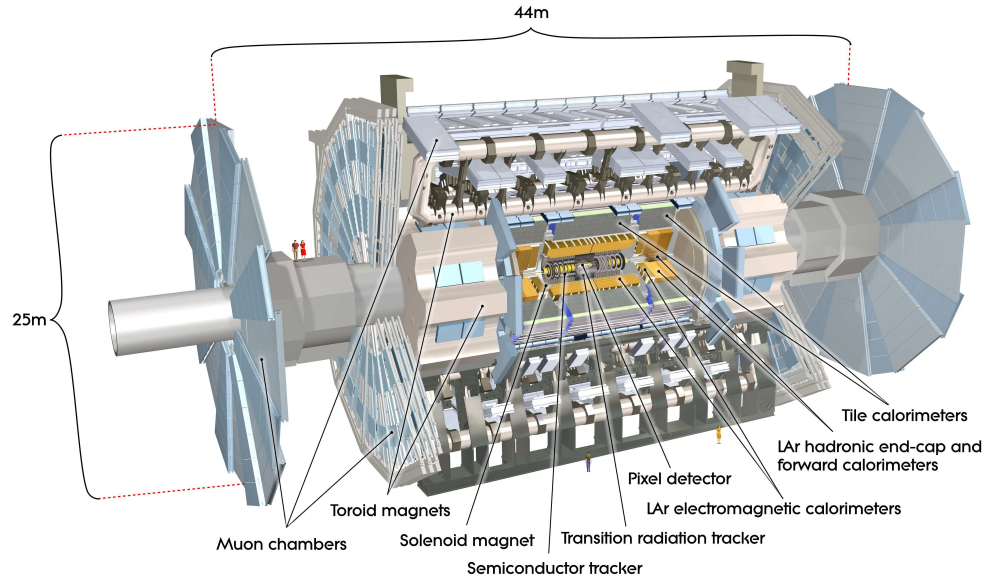


Figure 4.1: [3] Here we see a cut-away side view of the ATLAS detector with the major components labeled. Note that within each of these labeled components there may exist multiple different detector technologies. For scale two people in red are shown standing between the disk muon chambers on the left side of the figure.

417 the limits of the Standard Model in pursuit of answers to some of Humanities deepest
418 questions.

419 Located approximately 100 meters underground in a vast excavated chamber, the AT-
420 LAS detector rests its 7000 metric tonnes on a bed of concrete reinforced steel. Out of
421 it flows the signals of over 100 million electronic channels through a zip tied mass of
422 greater than 3000 kilometers of cabling. At its very center is one of the four interaction
423 points of the LHC, specifically Point 1, where the two counter circulating proton beams
424 are skillfully shaped and then collided by a series of magnets. The energetic particles
425 resultant from this collision then fly out in all directions into the bulk of the ATLAS
426 detector.

427 The first sub-system they meet is the Inner Detector (ID) and its many layers of strip
428 and pixel silicon detectors along with a transition radiation gaseous wire detector, all
429 bathed in the 2T magnetic field of the surrounding superconducting solenoidal magnet.
430 This system exploits the ionization of charged particles to track their curved trajectory
431 through the magnetic field. This curvature gives us charge information, a momentum
432 measurement, and precision 3D vertices crucial to the identification of the secondary
433 vertices of a b-hadron decay.

434 Outside of the solenoid the particles are faced with first the Electromagnetic and then
435 the Hadronic sampling calorimeters. Here, layers of scintillator and high radiation length
436 materials are implemented to measure the energy of electrons, photons, and hadrons.
437 As the goal is to completely absorb the energy of all outgoing particles the calorimeter

438 has a nearly 4π solid angle coverage.

439 Finally we have the muon system surrounding the calorimeter and equipped with its
440 own torroidal magnet system. Here the charged muon bends in the magnetic field
441 while leaving a trail of ionization in the muon spectrometer before exiting the detector
442 completely. Neutrinos are the only other standard model particle that leave the detector,
443 however they do so without detection. A depiction of the various particle interactions
444 with the different detector sub-systems can be seen in figure 4.2

445 In the following sections I will explain our choosen coordinate system and give a more
446 detailed reveiw of these 3 detector sub-systems.

447 4.1 ATLAS Coordinate System

448 Using the nominal interaction point as the origin, ATLAS uses a right handed coor-
449 dinate system where the positive x -axis points towards the center of the LHC ring,
450 the positive y -axis points upwards, and the positive z -axis is defined by the counter
451 clockwise circulating beam direction as viewed from above shown in figure 4.3 [3].

452 Using these coordinates we can define the physical momentum of the objects measured
453 as $\vec{p} = (p_T, p_z)$ with p_T being the momentum of the object in the transverse plane and
454 p_z the momentum along the beam axis. Given the cylindrical symmetry of ATLAS it
455 is desireable to define the polar angle θ from the beam axis with the $r - \phi$ plane being
456 perpendicular to that axis. Since the particles we observe are relativistically boosted

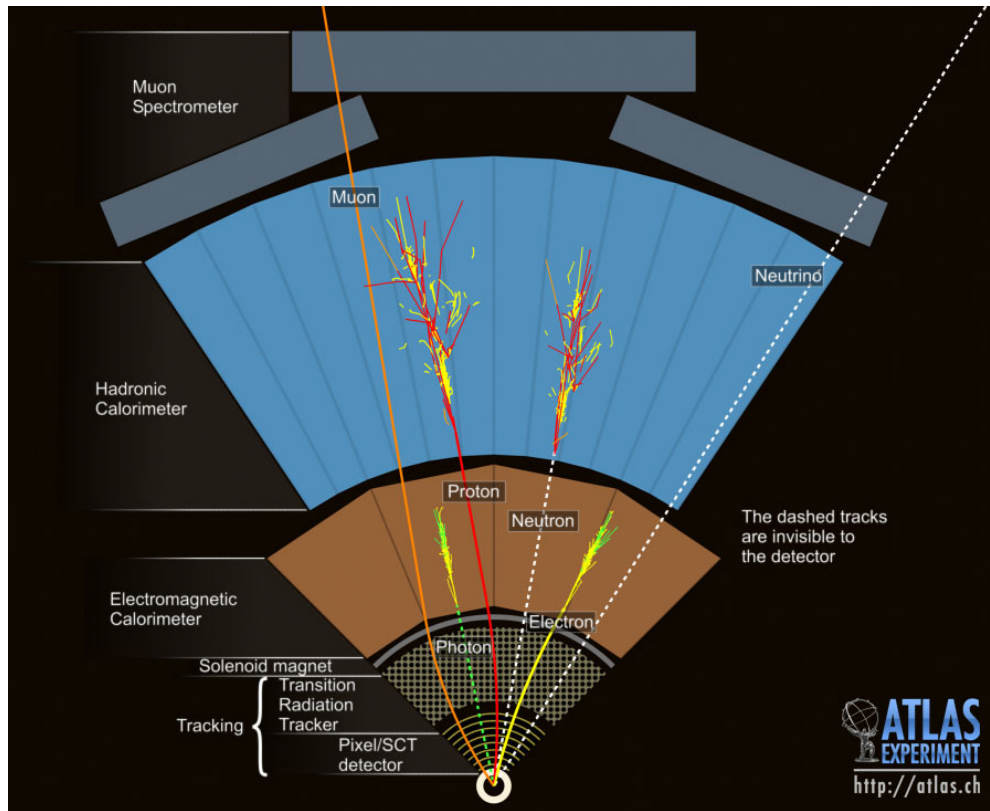


Figure 4.2: This slice of the ATLAS detector depicts how different particles interact with each component of the detector it crosses. A dashed line indicates no interaction while a solid line indicates interaction. Electrons (yellow/green) and charged hadrons (red) interact with the tracker and curve in the solenoid's magnetic field. Electrons and photons (yellow/green) are absorbed by the Electromagnetic calorimeter. All hadrons (red/yellow) are absorbed by the Hadronic calorimeter. The muons (orange) curve in both the solenoid and torroid magnetic fields before exiting the detector. Finally, the neutrinos (white) pass through the entire detector without interacting.

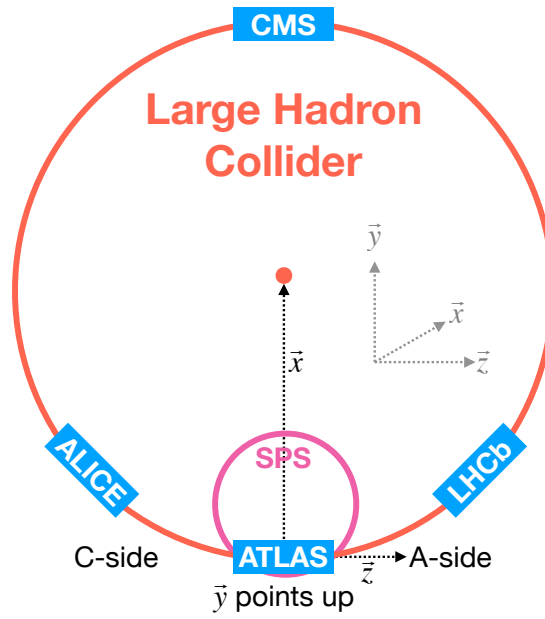


Figure 4.3: [4] A cartoon view of the the LHC from above showing the SPS, LHC and the four main experiments of the LHC: ATLAS, CMS, LHCb, and ALICE. The standard cartesian coordinate system is shown with its origin at the ATLAS interaction point, the positive x -axis towards the center of the LHC, the positive y -axis pointing upwards, and the positive z -axis pointing along the beamline towards the "A-side"

457 in the z -axis it is desirable to use the Lorentz invariant quantity pseudorapidity (η)
 458 defined in terms of the polar angle by

$$\eta = -\ln \tan \left(\frac{\theta}{2} \right). \quad (4.1)$$

459 where $\eta = 0$ is in the $x - y$ plane and larger values of $|\eta|$ being closer to the beam axis
 460 as can be seen in figure 4.4.

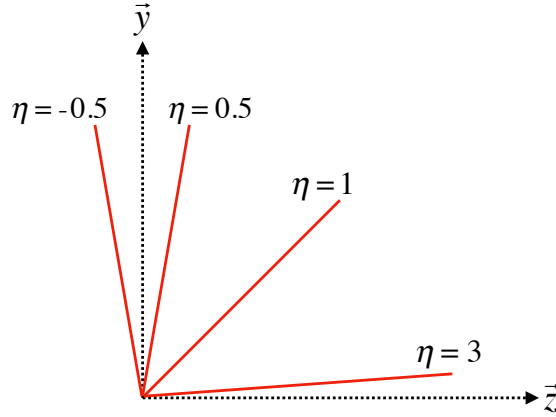


Figure 4.4: Modified from [4] this cartoon represents a selection of pseudorapidity (η) values overlaid with some cartesian coordinates (dashed black lines). The redlines are drawn for $\eta = \pm 0.5, 1.0, 3.0$

461 In this analysis the angular separation between objects in the detector is calculated and
 462 represented using the geometric quantity

$$\Delta R = \sqrt{(\Delta\eta)^2 + (\Delta\phi)^2} \quad (4.2)$$

4.2 Tracking with the Inner Detector

With its closest component, the insertable b-layer (IBL) [5], only 3.3 cm from the interaction point The Inner Detector (ID), shown in figure 4.5 [6, 7], faces the incredible challenge of providing precision momentum resolution and identification of both primary and secondary vertex measurements of charged tracks all while receiving the highest fluence.

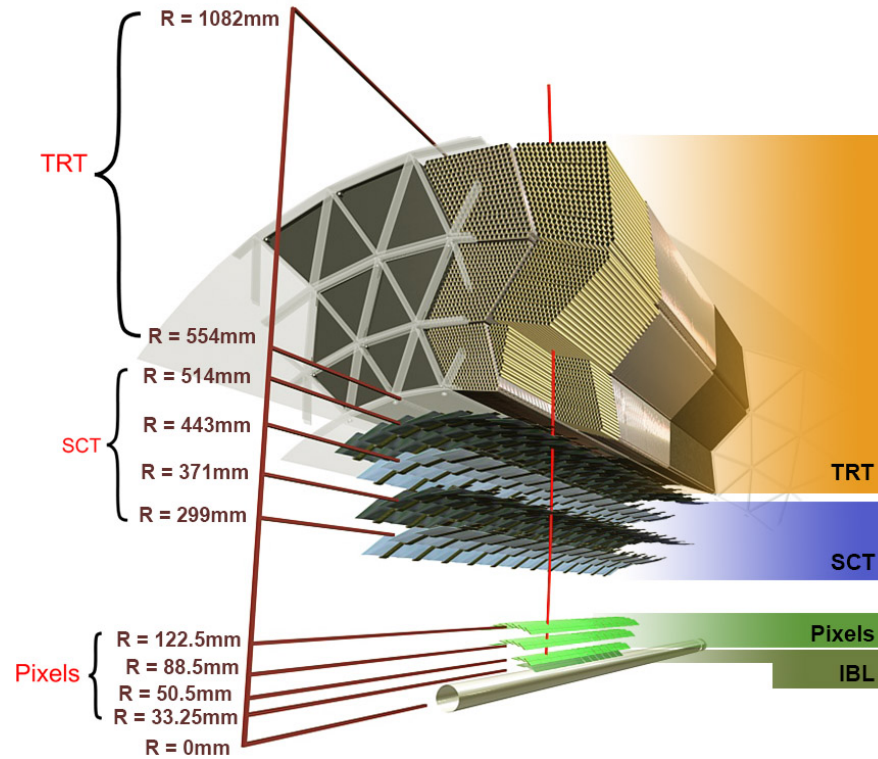


Figure 4.5: [5] Diagram of inner detector

It is designed to be very compact to reduce the probability of a particle decaying inside and to give precision measurements of the particles curvature in the 2T solenoidal

471 magnetic field. This leads to excellent momentum resolution above the nominal p_T
 472 threshold of 0.5GeV and within the pseudorapidity range of $|\eta| < 2.5$ as shown in figure
 473 4.6

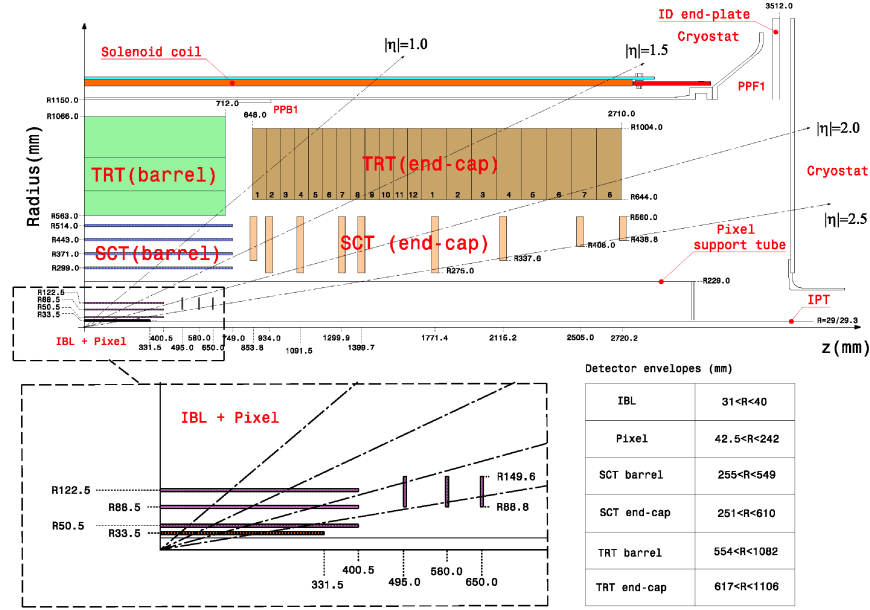


Figure 4.6: [8] Schematic of the Inner Detector including eta lines. Each component shown is cylindrically symmetric leading to a multi-layered detector.

474 The ID is composed of three different detector technologies for particle trajectory re-
 475 construction: The Pixel Detector, Semiconductor Tracker (SCT) and the Transition
 476 Radiation Tracker (TRT). These will be discussed in the following sections.

4.2.1 Pixel Detector

The ATLAS Pixel Detector [3], the innermost subdetector of the ID, is designed to give the best resolution possible as close as possible to the interaction point. This is accomplished using the 4 barrel layers and the 3 disks per endcap as indicated in figure 4.6. The inner most barrel layer, the IBL, has pixel dimensions of $50\mu\text{m}(\hat{\phi}) \times 250\mu\text{m}(\hat{z}) \times 200\mu\text{m}(\hat{r})$. For the other layers the dimensions are $50\mu\text{m}(\hat{\phi}) \times 400\mu\text{m}(\hat{z})$ for about 90% of the pixels and $50\mu\text{m}(\hat{\phi}) \times 600\mu\text{m}(\hat{z})$ for the others, all with a thickness of $250\mu\text{m}(\hat{r})$. This gives a total active area of 1.88m^2 collected through 92.4 million readout channels, more than half of the total number of channels for ATLAS. This detailed charged particle information very close to the interaction point is crucial not only for pattern recognition for track reconstruction, but also for the reconstruction of the primary and secondary vertices intrinsic to the decay of a b -hadrons, a critical element of the analysis presented in this thesis.

4.2.2 Semiconductor Tracker

Encompassing the Pixel Detector, the Semiconductor Tracker (SCT) [3] is composed of double sided silicon microstrips modules. Each side of the 4088 modules is constructed out of two silicon strip sensors that are daisy chained together. The result is 768 composite strips each 12.6cm with an inter-strip pitch of $80\mu\text{m}$. In the barrel the strips are aligned with the \hat{z} direction, while in the end caps they are aligned with the \hat{r} direction. In both cases the separation of the strips is constant in $\hat{\phi}$. The two sides are

497 rotated with respect to each other by $40\mu\text{m}$ to allow for position measurement along the
 498 length of the strip. These modules are then used to tile the 4 barrel layers and 9 disks
 499 per endcap (18 disks in total) as seen in figure 4.6. This design is chosen to ensure
 500 that each charged track interacts with 8 strip layers (equivalent to four space points).
 501 This information is used to further measure the momentum and impact parameter, and
 502 as well as vertex identification of charged particles.

503 **4.2.3 Transition Radiation Tracker**

504 The Transition Radiation Tracker [3], the outermost subdetector of the ID, provides
 505 tracking through the detection of transition radiation from ultra-relativistic charged
 506 particles for $\eta < 2.0$ using 350,000 drift tube channels also known as straws. The
 507 4mm diameter straws are filled with a 70% Xe, 27% CO₂, and 3% O₂ gas mixture
 508 and a $31\mu\text{m}$ diameter gold-plated tungsten wire anode at the center for the collection
 509 of the ionization signal. In the barrel 73 azimuthally symmetric layers of 144cm straws
 510 are oriented parallel to the beam pipe with an electrical division in the center of each
 511 allowing the two sides to be read out separately. For each endcap the straws are radially
 512 oriented in 160 symmetric planes each containing 768 37cm long drift tubes shown
 513 in figure 4.6. In both the barrel and the end caps polypropylene fibers (barrel) or
 514 foils (encaps) function as the transition radiation material which causes the relativistic
 515 charged particles to radiate and thus ionize the gas in the straw. The amount of
 516 transition radiation produced is proportional to the Lorentz factor meaning that lighter

517 particles (e.g. electrons) will produce more radiation. Thus, by defining a high and low
 518 threshold, we can identify tracks belonging to electrons by requiring they register more
 519 high-threshold hits. There are typically 36 TRT hits per charged track.

520 4.3 Calorimetry

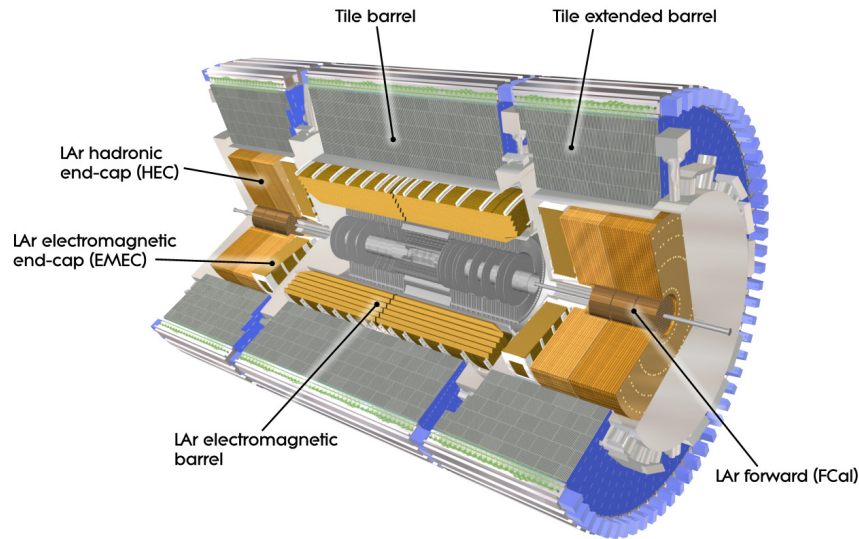


Figure 4.7: [3] A cutaway diagram of ATLAS's sampling calorimeters

521 Once the proton collision remnants have passed through the ID and it's surround-
 522 ing solenoid they enter into the ATLAS calorimeters depicted in figure 4.7. Sampling
 523 calorimeter technologies were choosen for their compact geometry and lower cost point.
 524 These are constructed by alternating layers of absorber, a dense material which reduces
 525 the incedent particles energy, and active material which produces a detectible signal
 526 when a partilce passes through. This means that the detected signal is only a fraction

527 of the total energy of the particle and thus requires a study of the calorimeter response
 528 for calibration purposes [9]. The first system, the Electromagnetic Calorimeter (EMC),
 529 is designed to measure the energy of electrons and photons which primarily lose their
 530 energy via bremsstrahlung and pair production electromagnetic interactions. Outside of
 531 the EMC is the Hadronic Calorimeter (HC) which is designed to measure the energy of
 532 jets of hadrons through their electromagnetic and strong interactions. These detectors
 533 cover the entire $|\eta| < 4.9$ range and provide complete containment of both Electromag-
 534 netic and Hadronic showers with higher granularity in the EMC for $|\eta| < 2.5$, the region
 535 matched to the ID, for precision measurements of electrons and photons. By instrument-
 536 ing this huge space in $|\eta|$ we can search for events with asymmetric energy deposits which
 537 imply the existence of a particle we didn't detect represented by missing transverse
 538 energy E_T^{miss} .

539 **4.3.1 Electromagnetic Calorimeter**

540 The innermost calorimeter, the Liquid Argon (LAr) Electromagnetic Calorimeter (EMC)
 541 [3], uses lead as the absorber and liquid argon as the active material in an "accordion
 542 geometry" as seen in figure 4.8. This geometry was chosen for uniform coverage in
 543 $\hat{\phi}$ due to its lack of un-instrumented cracks in the radial direction. The barrel region
 544 covers $|\eta| < 1.475$ and an end cap on each side covers $1.375 < |\eta| < 3.2$ each housed
 545 in their own cryostat. The barrel is composed of two half barrels with a 4mm gap at
 546 $z = 0$ and both end caps are divided into an inter wheel covering $2.5 < |\eta| < 3.2$ and

547 an outer wheel covering $1.375 < |\eta| < 2.5$.

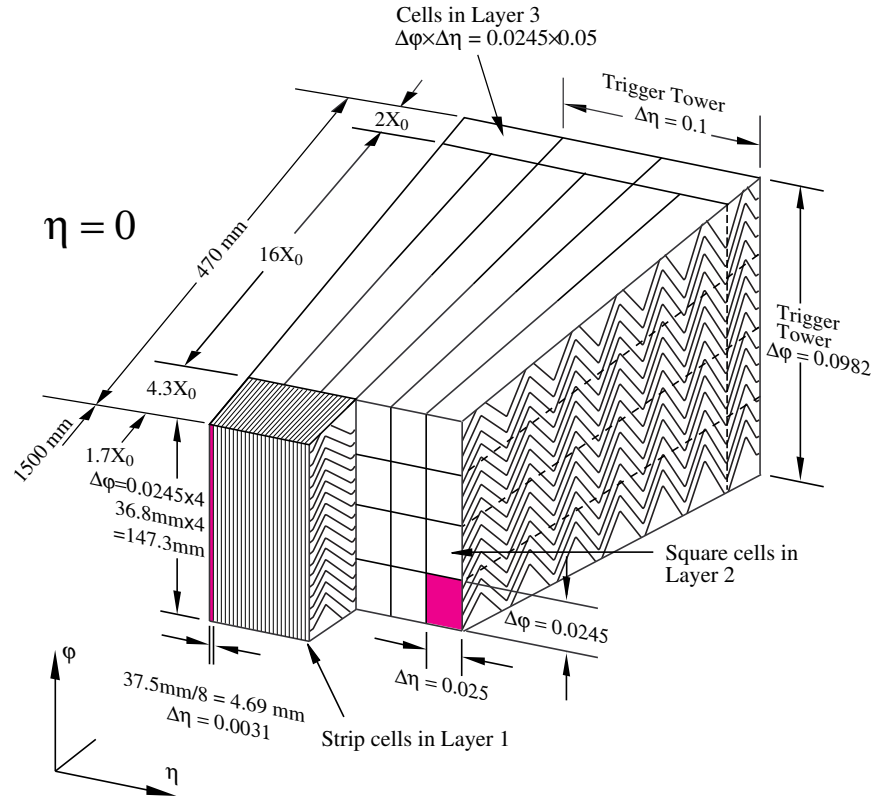


Figure 4.8: [3] Sketch of LAr EMC barrel module where the lead and liquid argon layers are visible in an accordion like geometry. Looking from the foreground to the back there are 3 different types of cells visible.

548 In the $|\eta| < 2.5$ region the EMC has 3 radial layers for precision physics measure-
 549 ments. Layer 1 consists of strip cells which are finely segmented with $\Delta\eta = 0.0031$
 550 and $\Delta\phi = 0.0245$ allowing for precision position resolution which gives discrimination
 551 power between a single γ deposit and the π^0 characteristic $\gamma\gamma$ deposit. Layer 2 , which
 552 collects the largest fraction of energy from electromagnetic shower, is segmented with

553 $\Delta\eta = .025$ and $\Delta\phi = 0.0245$. Layer 3 collects the tail of the electromagnetic shower
 554 using a coarser segmentation of $\Delta\eta = .05$ and $\Delta\phi = 0.0245$. Additionally, in the region
 555 $|\eta| < 1.8$ a thin pre-sampler, which contains no lead absorber, was placed in front of
 556 Layer 1 to allow for energy corrections due to losses upstream of the EMC. Combined
 557 the EMC is > 22 radiation lengths (X_0) in the barrel and $> 24 X_0$ in the end-caps,
 558 where a radiation length is the average distance an electron travels in a given material
 559 before losing $1/e$ of its original energy E_0 via bremsstrahlung radiation.

560 **4.3.2 Hadronic Calorimeter**

561 Directly outside the EMC envelope is the Hadronic Calorimeter (HC) system [3] which
 562 consists of three sampling calorimeter technologies: the Tile calorimeter, the LAr
 563 hadronic end-cap calorimeter (HEC) and the LAr forward calorimeter (FCal). Com-
 564 bined, these three subsystems give measurements of hadronic jet energies in the $0 <$
 565 $|\eta| < 4.9$ range. The tile calorimeter uses steel as the absorber layer and scintillating
 566 tiles as the active material and covers the region $|\eta| < 1.7$ with a barrel section flanked
 567 by two barrel extensions each divided azimuthally into 64 modules. These scintillator
 568 tiles are read out on two sides by wave-length shifting fibers connected to photomul-
 569 tiplier tubes as seen in figure 4.9. At $\eta = 0$ the total tile calorimeter thickness is 9.7
 570 nuclear interaction lengths (λ), where λ is the average distance a hadron travels before
 571 interacting inelastically with a nucleus.

572 The HEC is composed of two independent wheels per end-cap located just past the

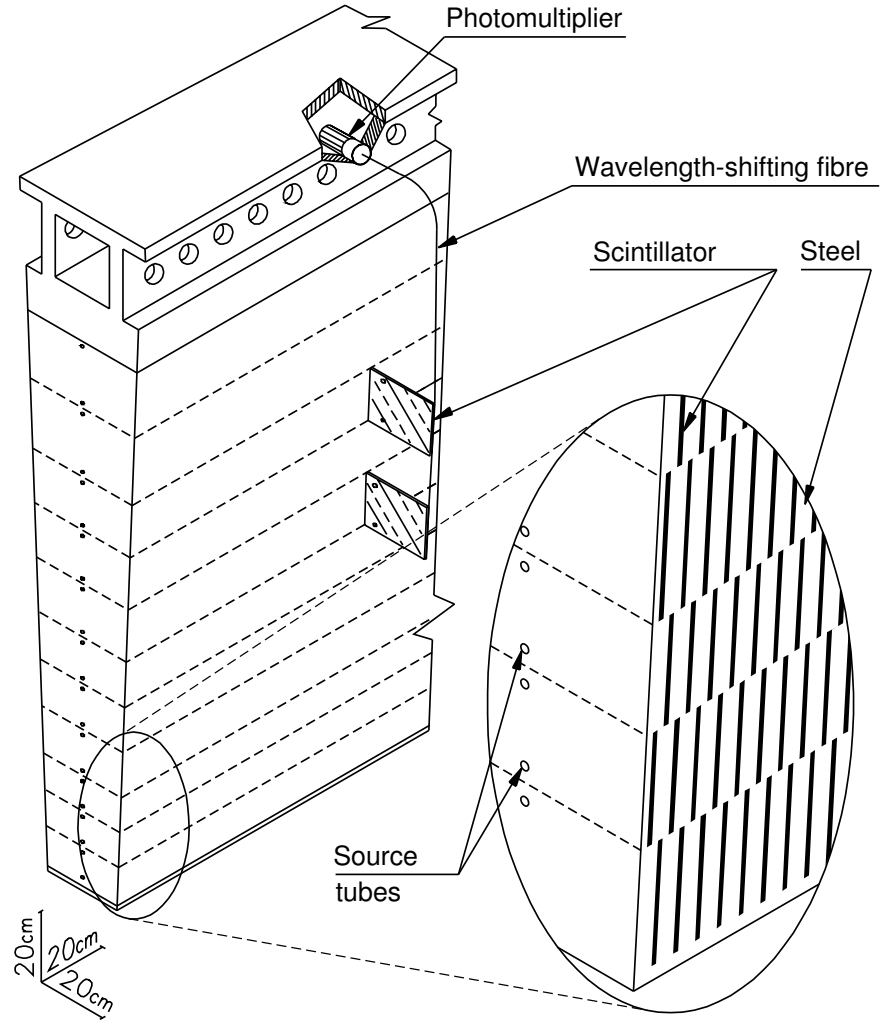


Figure 4.9: [3] Schematic of a tile calorimeter module including a depiction of the connection between the scintillator tile to the photomultiplier via a wavelength-shifting fibre.

573 EMC end-cap but sharing the same cryostat. This system uses copper as an absorber
 574 and liquid argon for the active material and covers the $1.5 < |\eta| < 3.2$ range using
 575 32 wdg-shaped modules per wheel. Finally, the FCal shares the same cryostat as the
 576 EMC and HEC end-caps and acts to extend the coverage of the combined calorimeter
 577 system to include the $3.1 < |\eta| < 4.9$ range. Each endcap contains 3 modules, the first
 578 an electromagnetic module (Copper/Liquid-Argon) which is followed by two hadronic
 579 modules which use (Tungsten/Liquid-Argon).

580 **4.4 Muon Spectrometer**

581 The ATLAS Muon Spectrometer (MS) [3], see figure 4.10, accomplishes tracking of
 582 charged particles in the $|\eta| < 2.7$ region for momentum reconstruction while also provid-
 583 ing triggering on charged particles in the $|\eta| < 2.4$ region. The magnetic field necessary
 584 for momentum reconstruction is provided by 3 air core torroid systems, one barrel tor-
 585 roid covering $|\eta| < 1.4$ and two endcap torroid systems which are inserted into the inner
 586 radius of the the barrel torroid to cover the $1.6 < |\eta| < 2.7$. The so called transition
 587 region $1.4 < |\eta| < 1.6$ between these two magnet systems is covered by a combination
 588 of the barrel and endcap torroid magnets. Similar to the ID the resolution is inversely
 589 proportional to the particle's incident momentum. Any muon with pT lower than 3GeV
 590 will never make it to the MS and thus will not be detected.

591 Precision tracking measurements for momentum reconstruction is accomplished using

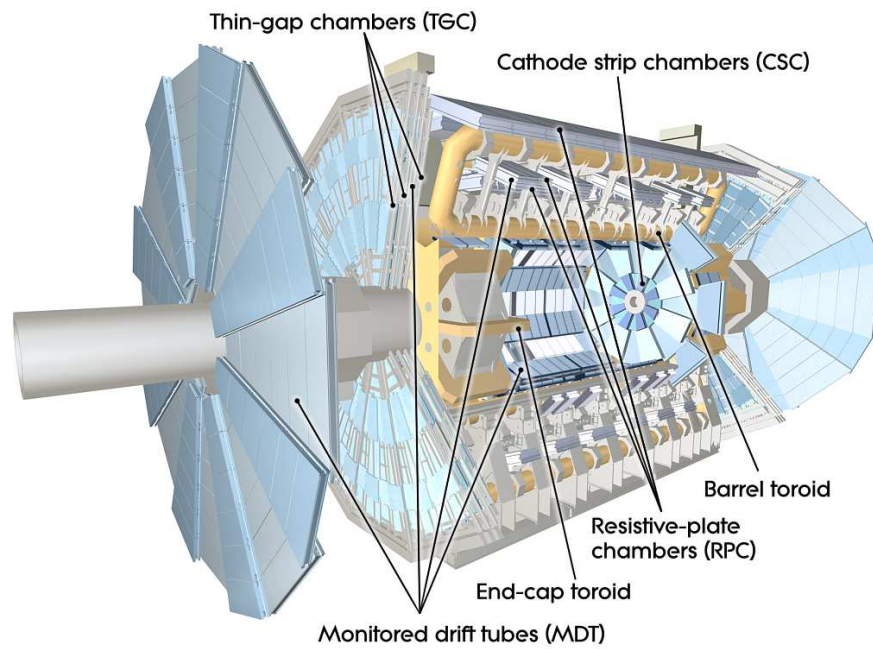


Figure 4.10: [3] A cut-away diagram of the ATLAS muon system and its many sub-detectors.

592 the Monitored Drift Tube chambers (MDTs) for $|\eta| < 2.0$ and using Cathode-Strip
593 Chambers (CSCs) for $2.0 < |\eta| < 2.7$. The MDT system consists of 1163 drift tube
594 chambers arranged in three to eight layers for varying η . The CSCs are designed to
595 withstand the higher rate and retain good time resolution using multiwire proportional
596 chambers with orthogonal segmented cathode planes.

597 The MS also gives nanosecond tracking information for triggering on muon tracks. This
598 is accomplished using Resistive Plate Chambers (RPC) in the barrel region $|\eta| < 1.05$
599 and Thin Gap Chambers (TGC) in the end-cap $1.05 < |\eta| < 2.4$ region. Both chamber
600 systems deliver a triggerable signal with a spread of 15–25 ns, thus providing the ability
601 to tag individual beam-crossings.

602 Chapter 5

603 Boosted Higgs at the LHC

604 Its July 4th, 2012 and the walls of building 500 are reverberating as Particle Physicists
605 around the world rejoice the discovery of the particle that gives all things mass, the
606 Higgs Boson.

607 **5.1 Physics beyond the Standard Model**

608 **5.2 Higgs Production Mechanisms**

609 **5.3 Branching Ratios**

610 **5.4 Discovery**

611 **5.5 Fermion Decay Modes**

612 **5.6 Boosted Higgs**

613

Part III

614

The HbbISR Analysis

615 **Chapter 6**

616 **Data and Simulation Preparation**

617 In order to compare data to theory ATLAS has developed an anlysis chain which runs
618 both real data and simulated samples through the same processing, assuring a final
619 result which is as comprable as possible.

620 **6.1 Data Used**

621 **6.2 Monte Carlo Samples**

622 Chapter 7

623 Physics Object Selection

624 After the ATHENA Digitization step both data and monte carlo have the same format,
625 representing the three dimentional energy deposits. In order to analyze these deposits
626 they are cleaned, clustered and checked for overlap resulting in physics objects useful
627 for our specific analysis.

628 **7.1 Calorimeter Jets**

629 **7.2 Track Jets**

630 **7.3 Fat Jets**

631 **7.4 B-tagged Jets**

632 **7.5 Muons**

633 **7.6 Overlap Removal**

634 Chapter 8

635 Event Selection

636 Having created our physics objects we begin to make selections of what types of events
637 we want to consider given the goal of our analysis. In our boosted topology this means
638 considering things like momentum, jet collection efficiencies and background rejection.

639 8.1 Selected Triggers

640 8.2 Pre-selection Studies

641 8.3 Signal Selection

642 8.4 Optimisation

643 Chapter 9

644 Background Estimation

645 The dominant background was QCD. I worked on the $t\bar{t}$ control region. The V_{qq}
646 and single top backgrounds were estimated from monte carlo.

647 9.1 Multi-jet QCD estimation

648 9.2 $t\bar{t}$ control region

649 9.3 Single top estimation

650 9.4 Hadronic vector boson channel

651 **Chapter 10**

652 **Systematic Uncertainties**

653 **10.1 Theoretical Uncertainties**

654 **10.2 Experimental Uncertainties**

655 **Chapter 11**

656 **Statistical Fit**

657 The statistical fit in our analysis was accomplished using a framework developed for
658 Higgs searches.

659 **11.1 Profile Likelihood Function**

660 **11.2 Fit Configuration**

661 **11.3 Statistical Tests**

662 **Chapter 12**

663 **Results**

664 **12.1 Expectations**

665 **12.2 Statistical Analysis Results**

666 **12.3 Measurements and Limits**

667

Part IV

668

Conclusion

669 Chapter 13

670 Conclusion

671 I conclude that this section is the conclusion

Bibliography

- [1] Lyndon Evans and Philip Bryant. “LHC Machine”. In: *JINST* 3 (2008), S08001. DOI: 10.1088/1748-0221/3/08/S08001 (cit. on p. 13).
- [2] Chris Llewellyn Smith. “Genesis of the Large Hadron Collider”. In: *Phil. Trans. Roy. Soc. Lond.* A373.2032 (2014), p. 20140037. DOI: 10.1098/rsta.2014.0037 (cit. on p. 13).
- [3] ATLAS Collaboration. “The ATLAS Experiment at the CERN Large Hadron Collider”. In: *JINST* 3 (2008), S08003. DOI: 10.1088/1748-0221/3/08/S08003 (cit. on pp. 24, 26, 32–40).
- [4] Giordon Holtsberg Stark. “The search for supersymmetry in hadronic final states using boosted object reconstruction”. Presented 26 Apr 2018. May 2018. URL: <https://cds.cern.ch/record/2317296> (cit. on pp. 28, 29).
- [5] Karolos Potamianos. *The upgraded Pixel detector and the commissioning of the Inner Detector tracking of the ATLAS experiment for Run-2 at the Large Hadron Collider*. Tech. rep. ATL-PHYS-PROC-2016-104. 15 pages, EPS-HEP 2015 Proceed-

- 687 ings. Geneva: CERN, Aug. 2016. URL: <https://cds.cern.ch/record/2209070>
 688 (cit. on p. 30).
- 689 [6] *ATLAS inner detector: Technical Design Report, 1*. Technical Design Report AT-
 690 LAS. Geneva: CERN, 1997. URL: <http://cds.cern.ch/record/331063> (cit. on
 691 p. 30).
- 692 [7] S Haywood et al. *ATLAS inner detector: Technical Design Report, 2*. Technical
 693 Design Report ATLAS. Geneva: CERN, 1997. URL: [https://cds.cern.ch/](https://cds.cern.ch/record/331064)
 694 [record/331064](https://cds.cern.ch/record/331064) (cit. on p. 30).
- 695 [8] B. Abbott et al. “Production and integration of the ATLAS Insertable B-Layer”.
 696 In: *JINST* 13 (2018), T05008. DOI: 10.1088/1748-0221/13/05/T05008. arXiv:
 697 1803.00844 [physics.ins-det] (cit. on p. 31).
- 698 [9] Christian Wolfgang Fabjan and F Gianotti. “Calorimetry for Particle Physics”.
 699 In: *Rev. Mod. Phys.* 75.CERN-EP-2003-075 (Oct. 2003), 1243–1286. 96 p. DOI:
 700 10.1103/RevModPhys.75.1243. URL: <https://cds.cern.ch/record/692252>
 701 (cit. on p. 35).

702 **Appendix A**

703 **Hadronic Vqq Sherpa Studies**

704 Ancillary material should be put in appendices, which appear after the bibliography.